Forest vulnerability to drought controlled by bedrock composition

Authors
Russell P. Callahan[1], Clifford S. Riebe[1], Leonard S. Sklar[2], Sylvain Pasquet[3], Ken L. Ferrier[4], W. Jesse Hahm[5], Nicholas J. Taylor[1], Dario Grana[1], Brady A. Flinchum[6], Jorden L. Hayes[7], W. Steven Holbrook[8]
Affiliations
[1]Department of Geology and Geophysics, University of Wyoming, Laramie, WY 82071, USA
[2]Department of Geography, Planning and Environment, Concordia University, Montréal, Quebec, H3G 1M8, Canada
[3]Université Paris Cité, Institut de physique du globe de Paris, CNRS, F-75005 Paris, France
[4]Department of Geoscience, University of Wisconsin-Madison, Madison, WI 53706, USA
[5]Department of Geography, Simon Fraser University, Burnaby, British Columbia V5A 1S6, Canada
[6]Department of Environmental Engineering and Earth Sciences, Clemson University, Anderson, SC 29625, USA
[7]Department of Earth Sciences, Dickinson College, Carlisle, PA 17013, USA
[8]Department of Geosciences, Virginia Polytechnic Institute and State University, Blacksburg, VA 24061, USA
Corresponding author: Russell Callahan (rucallah@ucsc.edu)

Abstract
Forests are increasingly threatened by climate-change-fueled cycles of drought, dieback, and wildfires. However, for reasons that remain incompletely understood, some forest stands are more vulnerable than others, leaving a patchwork of varying dieback and wildfire risk after drought. Here, we show that spatial variability in forest drought response can be explained by differences in underlying bedrock. Our analysis links geochemical measurements of bedrock composition, geophysical measurements of subsurface weathering, and remotely sensed changes in evapotranspiration during the 2011-2017 drought in California. We find that evapotranspiration plummeted in dense forest stands rooted in weathered, nutrient-rich bedrock. In contrast, relatively unweathered, nutrient-poor bedrock supported thin forest stands that emerged unscathed from the drought. By influencing both subsurface weathering and nutrient supply, bedrock composition regulates the balance of water storage and demand in mountain ecosystems. However, rather than enhancing forest resilience to drought by providing more water storage capacity, bedrock with more weatherable and nutrient-rich minerals induced greater vulnerability by enabling a boom-bust cycle in which higher ecosystem productivity during wet years drives excess plant water demand during droughts.

Main text
The 2011–2017 California drought killed over 140 million trees[1], leaving swaths of desiccated vegetation[2] that have fueled some of the most ecologically[3] and economically[4] devastating wildfires on record. Although tree death after the drought was widespread, some stands emerged unscathed or exhibited temporary drought stress, creating meter-to-kilometer-scale patchiness in forest dieback[5,6] spanning the spectrum of forest drought response, from leaf browning to complete topkill[7,8]. This patchiness cannot be fully explained by differences in topography, climate, or forest structure[9,10]. Bedrock mineralogy also varies over the scale of dieback patchiness, suggesting that spatial variations in dieback can be explained by differences in bedrock composition. For example, forests on substrates derived from bedrock containing abundant weatherable minerals[11,12] may be buffered against reduced precipitation by water stored in highly weathered and thus highly porous substrates[13]. Alternatively, highly weathered substrates, with high water storage capacity, may make forests more prone to dieback by promoting high plant growth during wet years, leading to plant-water demand that cannot be satisfied during drought[14]—a phenomenon known as structural overshoot[7,15]. Such boom-bust cycles of growth and dieback may also occur where forest productivity is enhanced by high concentrations of plant-essential nutrients in bedrock.

We tested these hypotheses by quantifying the relationship between patchy dieback and bedrock composition at three geologically distinct sites with forests spanning a 15-fold range in evapotranspiration-based estimates of drought-related dieback (Fig. 1; Extended Data Fig. 1; Methods). The site-to-site differences in dieback cannot be explained by differences in average climate, climate seasonality, or microclimate. The sites lie within a 4500 m radius (Fig. 1a), experience the same weather patterns, and share a similar average climate (Extended Data Table 1). They also have similar elevations on ridgetops with similar distributions of hillslope gradient and aspect (Extended Data Fig. 2). Hence, they have similar aridity (Fig. 1d), climate seasonality, and snowmelt timing, which could otherwise influence drought vulnerability[16]. In contrast, the sites lie within three geochemically distinct plutons (Methods) that vary both in the abundance of mafic minerals (e.g., biotite, Extended Data Fig. 3) that promote subsurface weathering and the concentration of nutrients (e.g., phosphorus) that promote plant growth[17] and thus water demand (Fig. 1b). Thus, our study exploits the similarity in climate, variability in bedrock composition, and patchiness of dieback across our sites as a natural experiment for isolating subsurface weathering and nutrient supply[18] as geologic controls on drought response.

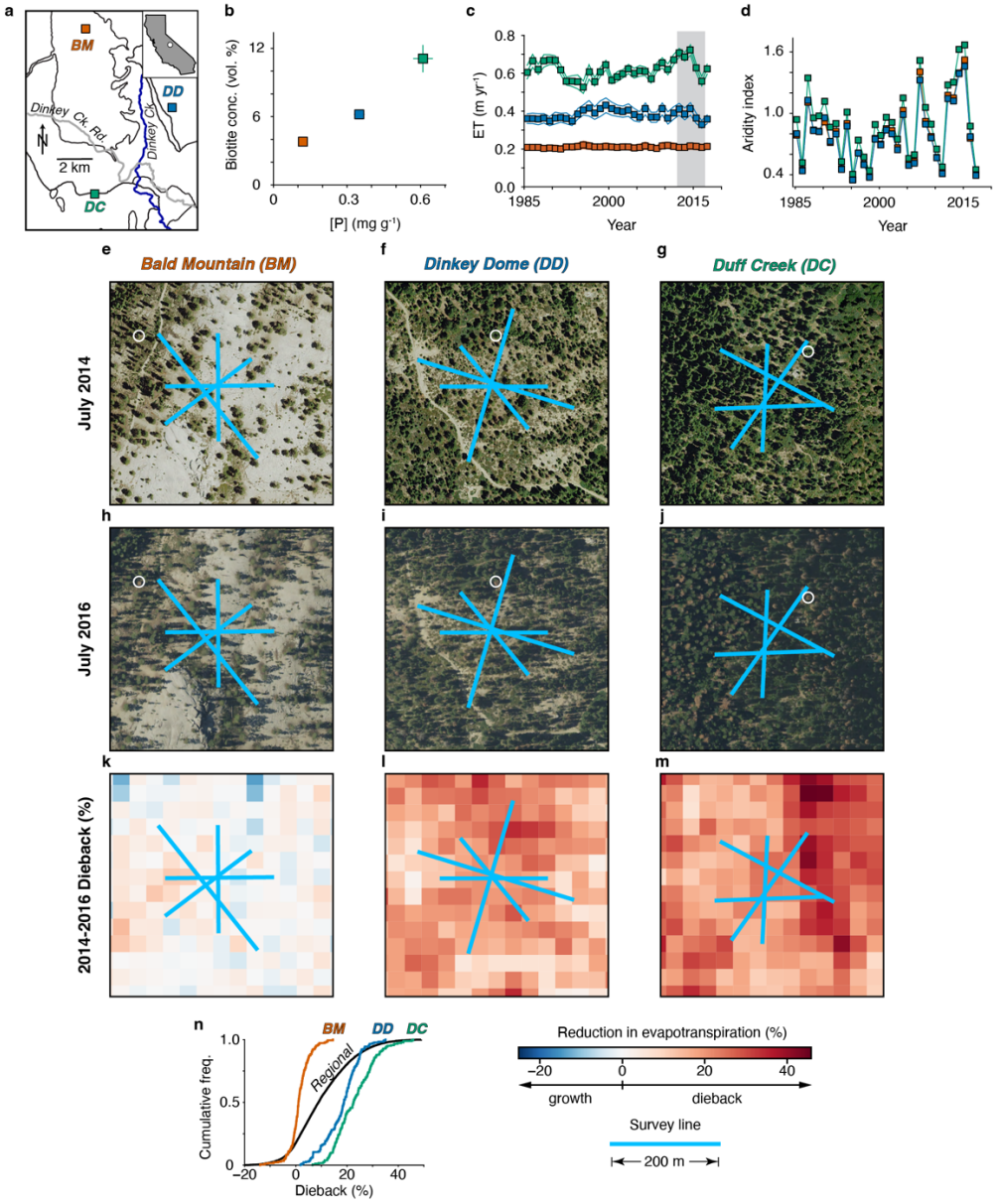

Fig. 1 | Differences in dieback, forest cover, and bedrock composition. a, Bald Mountain (BM), Dinkey Dome (DD), and Duff Creek (DC) have differing bedrock (black outlines)[19] but similar elevation, climate (Extended Data Table 1), and erosion rates[20]. **b,** Biotite concentration correlates with phosphorus concentration in bedrock ([P]). **c**, Yearly average evapotranspiration (lines show 95% CI) from Landsat-based normalized difference vegetation index (NDVI; Methods). Dieback lagged start of 2011–2017 drought (gray box) by three years. **d**, Aridity index (potential evapotranspiration divided by precipitation) varies from year to year, but is similar across the sites each year. National Agricultural Imagery Program (NAIP) imagery from before **e–g,** and after, **h-j** widespread dieback. **k-m,** Spatial variations in percentage change in evapotranspiration from 2014 to 2016 (Methods) match observations of leaf browning and tree mortality from aerial imagery, supporting reduction in evapotranspiration as a measure of dieback. **n,** Distribution of dieback differs markedly between sites ($p<0.0001$; Kolomogorov-Smirnov test with Bonferroni correction for 3 samples) and collectively spans 94% of range in dieback at similar elevations in surrounding region (black line; Extended Data Fig. 1). Colors throughout figure correspond to site labels in **a**.

From the isolated, sparsely populated tree stands on Bald Mountain to the denser forests at Duff Creek, tree canopy cover increases fivefold (Fig. 1e–j), average evapotranspiration increases threefold (Fig. 1c), and year-to-year variability in evapotranspiration increases tenfold (Extended Data Table 1). The sites also differ in tree species, with slow-growing, drought-tolerant Jeffrey pine[21] dominating at Bald Mountain and faster-growing white fir, sugar pine, and ponderosa pine at Dinkey Dome and Duff Creek (Extended Data Fig. 4). The site-to-site differences in species and evapotranspiration cannot be explained by differences in precipitation or potential evapotranspiration, because aridity index does not vary across the sites in any given year, even as it varies from year to year (Fig. 1d). Instead, site-to-site differences in species distribution, average evapotranspiration, and evapotranspiration variability all correlate with differences in bedrock composition. In particular, bedrock with higher biotite concentrations had higher dieback in overlying vegetation (Fig. 1m), contrary to the hypothesis that greater concentrations of weatherable minerals should buffer forests against reduced water inputs during drought by creating greater water storage capacity.

This counterintuitive finding raises questions about links between bedrock composition and dieback that cannot be answered with the geologic maps and remote sensing data alone. Do differences in biotite concentration drive differences in weathering and thus water storage capacity that are big enough to affect overlying forests? If so, are forests nonetheless more vulnerable where weathering is greater, because the buffering effect of greater water storage capacity is overwhelmed by higher plant water demand? Finally, if higher plant water demand dominates in making forests more vulnerable to drought, is it because of higher bedrock nutrient content, greater water availability in wet years (due to greater storage capacity), or both? Answering these questions requires measurements of subsurface weathering at the scale of patchiness in forest drought response. However, subsurface weathering has typically only been measured from shallow soil pits[22], which do not characterize vital water storage capacity at depth[23–25], and from deeper but isolated boreholes[26,27], which are rarely numerous enough to quantify spatial variability in subsurface weathering[28].

Bedrock controls on water storage and plant water demand

To investigate how water-storage capacity over the full thickness of weathered rock and soil varies at the 10^1–10^2 m scales of patchy dieback, we quantified how subsurface porosity varies with depth using hillslope-spanning seismic refraction surveys at each site (Methods). Porosity (in m^3/m^3) was derived from a rock physics model calibrated in previous work using push-core data from a nearby site (Methods).

We quantified total subsurface water-storage capacity by integrating porosity over depth. The resulting measurements of total unit pore volume (in m^3/m^2) quantify the depth of water required to fill all voids in a vertical column of weathered soil and saprolite[29] (Methods; Extended Data Fig. 5). Because the geophysical measurements of porosity have a resolution of 10^0–10^1 m, we can aggregate them into

estimates of water storage capacity averaged over the ~40,000 m^2 scale of each survey site and the 900-m^2 scale of Landsat pixels (Fig. 1k-m).

Joint distributions of porosity and depth aggregate the geophysical data at the scale of each site[28], revealing sharp contrasts in subsurface weathering that correspond as expected to site-to-site differences in bedrock composition (Fig. 2a-c). Porosity, which combines effects of physical and chemical weathering[30,31], increases with weatherable mineral concentrations across the sites. For example, mean porosity in the top 2 meters, where roots are concentrated, increases from ~0.37 m^3/m^3 at Bald Mountain, where biotite concentrations are lowest, to ~0.54 m^3/m^3 at Duff Creek, where they are highest (Fig. 2d). Biotite concentrations also correlate positively with unit pore volume (Fig. 2e)—i.e., the sum of porosity integrated over the entire soil-saprolite profile, including deep storage space that may be vital to forests during drought[32]. These differences in unit pore volume in part reflect differences in the combined thickness of soil and saprolite, which increases from 1.5±0.1 m (mean±s.e.m) at Bald Mountain, to 7.7±0.3 m at Duff Creek (Fig. 2f). Together, these results support the hypothesis that site-to-site differences in forest cover (Fig. 1e-j) are driven by differences in water storage capacity that are regulated by weatherable mineral concentrations in bedrock (Fig. 2g). However, the strong correlation between weatherable mineral and bedrock nutrient concentrations between the sites (Fig. 1b) implies that either or both of these factors could explain the site-to-site differences in forest cover[17,33].

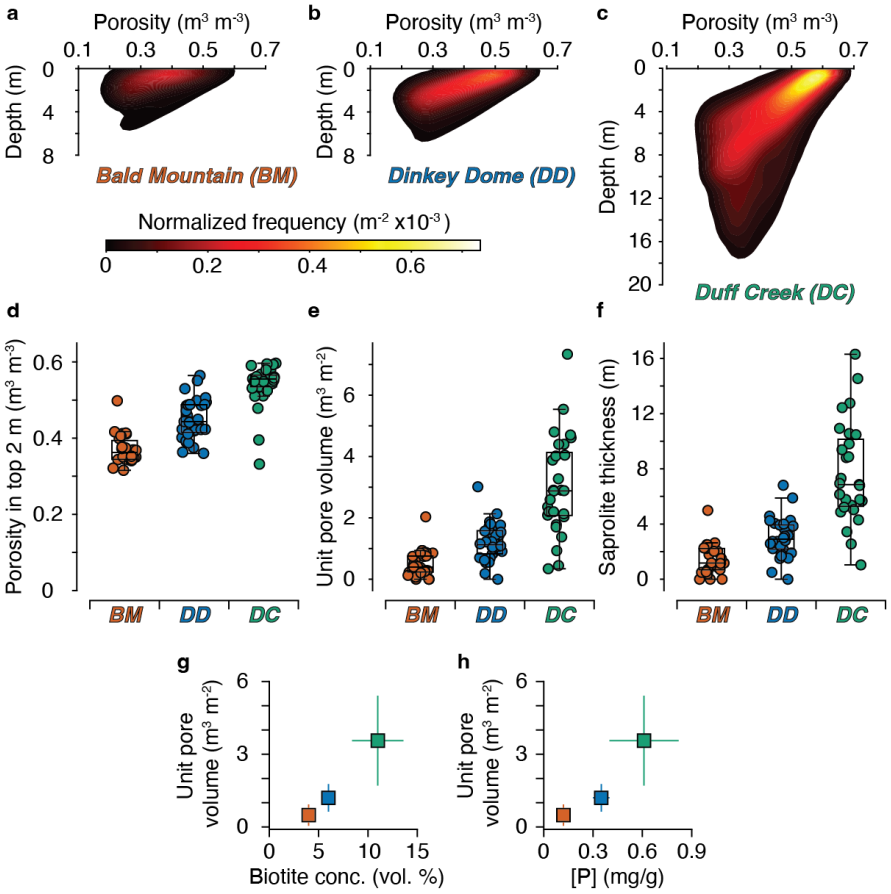

Fig. 2 | Porosity and water storage capacity controlled by bedrock composition. **a–c**, Joint distribution of porosity and depth from rock physics model of seismic refraction data and condensed into site-wide porosity profiles[28] (Methods). Frequency distributions of **d,** mean porosity in top 2 m; **e**, unit pore volume, the depth of water required to fill pores in soil and saprolite (Methods); and **f**, combined thickness of soil and saprolite, material with V_P <1.1 km s^{-1} [28,34]. Circles represent averages over

individual Landsat pixels. Box plots show median (center line), first and third quartile (box), and whiskers that extend up to 1.5 times the interquartile range past the first and third quartile. Average (±1 s.d.) pore volume per unit area increases with average bedrock concentration of biotite (**g**) and phosphorus (**h**).

Analysis of Landsat data provides evidence that both factors contributed to differences in pre-drought evapotranspiration (Fig. 3). Evapotranspiration from remote sensing increases with unit pore volume from geophysical surveys (Fig. 3a, dashed line), suggesting that differences in forest cover and thus evapotranspiration are regulated by water storage capacity. Moreover, each site has a statistically distinct, vertically offset trend (Fig 3a, colored lines; Extended Data Table 2), indicating that locations at Duff Creek, Dinkey Dome, and Bald Mountain with the same unit pore volume have different evapotranspiration rates ($p<0.0001$). Hence, the variation in forest productivity across our sites cannot be explained by water storage capacity alone.

An additional control on forest productivity may be variations in bedrock nutrient concentrations[17]. Vegetation on the nutrient-rich Duff Creek bedrock, had higher evapotranspiration per unit pore volume than vegetation at Dinkey Dome (Fig. 3a), which in turn had higher evapotranspiration than vegetation growing on the nutrient-poor Bald Mountain bedrock[17]. Lower evapotranspiration at Bald Mountain may also reflect species-related differences in evapotranspiration per unit pore volume (Fig. 3a). However, the species differences across our sites correlate with bedrock nutrient concentration and water storage capacity, and cannot be explained by climate. This suggests that any species-related differences in evapotranspiration are indirectly controlled by differences in bedrock composition.

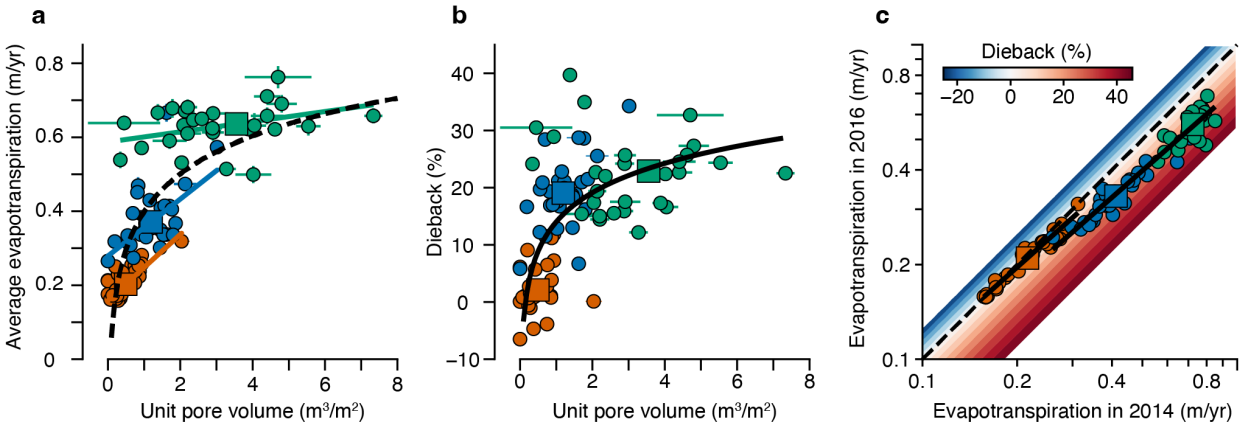

Fig. 3 | Plant water demand, water storage potential, and drought response. a, Pre-drought (2007–2011 average) evapotranspiration versus unit pore volume, showing averages (±1 s.e.m.) by site (squares) and pixel (circles) with linear-log fit to all data (dashed; $r^2=0.75$) and statistically distinct linear relationships for Duff Creek (green), Dinkey Dome (blue), and Bald Mountain (red). **b,** Dieback increases with unit pore volume ($r^2=0.51$). **c**, Evapotranspiration in 2016 along survey lines was generally lower than evapotranspiration in 2014 and thus plots below dashed 1:1 line, reflecting dieback during the drought. A three-parameter log-log regression, with a slope, intercept, and offset between Bald Mountain and the other two sites (Methods; Extended Data Table 3) yields slope=0.88±0.02, indicative of structural overshoot, in which locations with higher pre-dieback evapotranspiration (and higher forest productivity) had disproportionately higher dieback (colorbar).

Bedrock controls on dieback

The bedrock-driven differences in evapotranspiration (Fig. 3a) correlate with observed differences in dieback during the 2011–2017 drought (Fig. 1). Dieback was greatest between 2014 and 2016 across the

sites (Fig. 1c,k-m, Extended Data Fig. 6) and was more pronounced at locations with higher unit pore volume (Fig. 3b). Those locations also had greater evapotranspiration and thus greater plant water demand before the drought (cf. Figs. 3a,b). Hence, dieback increased with pre-dieback plant water demand (Fig. 3b), despite the greater storage capacity of locations with greater demand (Fig. 3a). This suggests that forests with more vegetation can be more vulnerable to dieback during drought due to structural overshoot, even when vegetation is anchored in substrates with more subsurface weathering.

To directly show how vulnerability increases with forest productivity, we plot post- versus pre-dieback evapotranspiration in log-log space, revealing the fractional reduction in evapotranspiration with increasing demand (contours in Fig. 3c). The data can be fit with a three-parameter log-log regression, with a slope, an intercept, and an offset between Bald Mountain and the other two sites (Methods; Extended Data Table 3) that is indicative of 9±2% ($p=0.0002$) greater dieback at Dinkey Dome and Duff Creek for a pre-dieback evapotranspiration of 0.3 m/yr (Fig. 3c). We hypothesize that this offset reflects the drought tolerance of slow-growing Jeffrey pine[21], which dominates at Bald Mountain because it is adapted to the site's low bedrock nutrient content and low water-storage capacity. If this is the case, then dieback was partly controlled by differences in species distributions that are regulated by bedrock composition through its influence on nutrient supply and subsurface weathering.

The slope in the three component regression is 0.88±0.02, which is significantly less than 1.00 ($p<0.0001$), the minimum slope consistent with the hypothesis that denser forests are equally or less vulnerable to drought because of greater water storage capacity. Contrary to that hypothesis, we observe a disproportionate increase in relative dieback with increasing pre-dieback evapotranspiration and thus with increasing water storage capacity. This is true within each site and across the three sites combined, irrespective of site-to-site differences in tree species. Hence, at all sites, including Bald Mountain, dieback correlates strongly with demand (Fig. 3c), suggestive of widespread structural overshoot that is regulated by differences in subsurface weathering. These results emerge whether dieback is measured as a percentage change in evapotranspiration (Fig. 3c) or NDVI measurements (Extended Data Fig. 7).

To determine whether bedrock control of dieback during the California drought was widespread, we quantified the reduction in evapotranspiration from 2014 to 2016 at 18 granitic sites selected from a 1425-m-wide elevation band spanning a 186-km-long transect through the Sierra Nevada (Fig. 4a). The results are consistent with structural overshoot (slope<1.0 in Fig. 4b), extending the findings from the three main sites (Fig. 3c) to the surrounding region. The regional analysis also supports strong bedrock control of structural overshoot, despite site-to-site differences in climate due to differences in latitude and elevation. Site-to-site differences in bedrock phosphorus concentration [P] alone can explain 42% of the variance ($p=0.004$) in both evapotranspiration (Fig. 4c) and dieback (Fig. 4d). Meanwhile, neither mean annual temperature (MAT) nor precipitation (MAP) alone explain more than 14% of the variance in either evapotranspiration or dieback ($p>0.1$). However, when [P], MAT, and MAP are combined in multiple linear regression, they explain 67% of the variance in evapotranspiration ($p=0.001$) and 65% of the variance in dieback ($p=0.002$), and the regression slopes for [P], MAT, and MAP in both regressions are all statistically significant ($p<0.04$). Collectively, the regression statistics in Extended Data Table 3 suggest that bedrock composition is the dominant control on structural overshoot-driven dieback not only at the three sites with similar climates (Fig. 3), but also across a broader range of mid-elevation climates in Sierra Nevada (Fig. 4).

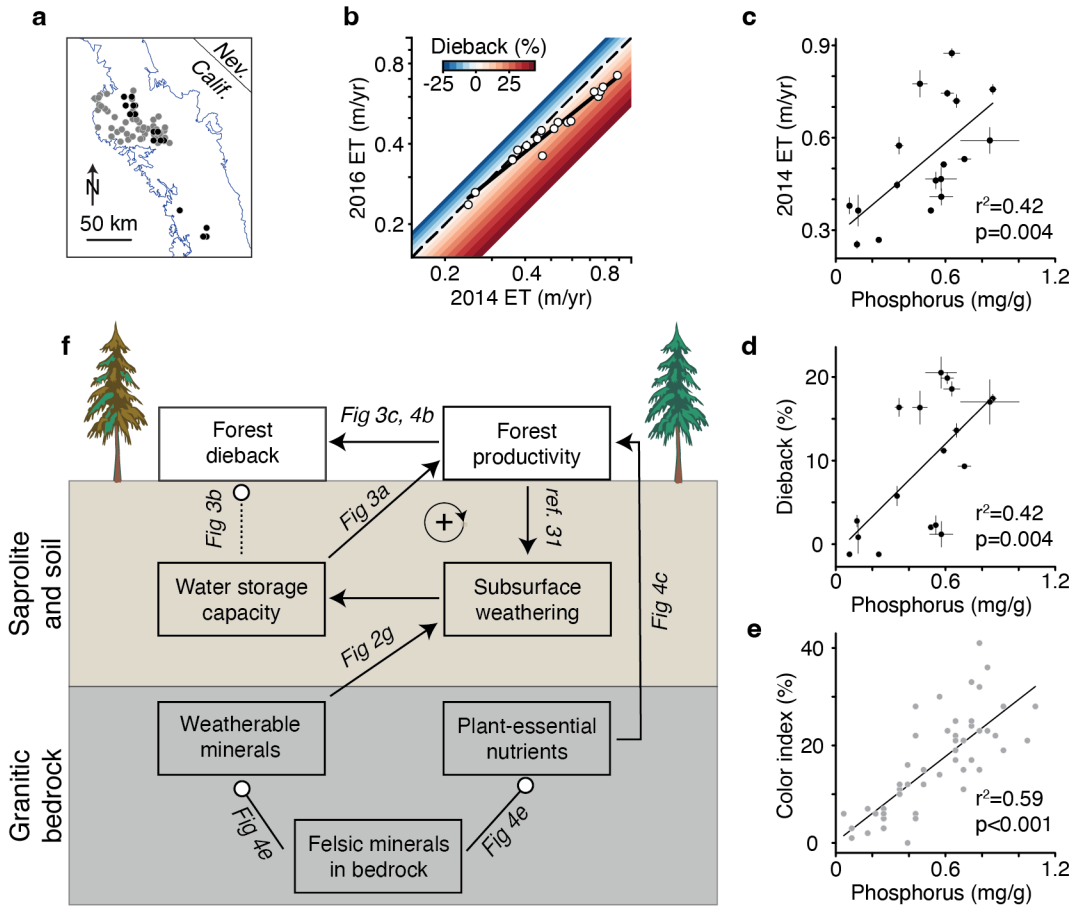

Fig. 4 | Bedrock control on drought response in the Sierra Nevada. a, Bedrock sample locations from ref. ([17]) (black) and ref. ([35]) (gray) within the Sierra Nevada Batholith (blue outline). **b**, Dieback increased disproportionately with average evapotranspiration (ET) in 2014 ($p<0.001$), implying widespread bedrock control on dieback. This is confirmed by positive correlations between [P] and both pre-dieback evapotranspiration **c**, and dieback **d** (average±1 s.e.m.). **e,** Mafic mineral concentrations in bedrock (color index, in volume %) increase with [P] after ref. ([35]). **f,** Systems diagram showing links between bedrock composition and forest dieback in the critical zone (conceptualized in background image). Positive and negative couplings are arrows and lines terminated by circles, respectively. Labels refer to supporting results. Dashed connector near top shows hypothesized buffering of dieback by storage capacity, an effect that was overwhelmed here by the positive coupling between forest vulnerability and water demand. Based on regression offset in Fig. 3c, we hypothesize that the strength of the coupling between forest productivity and dieback depends on species distribution, which in turn depends on bedrock composition.

Although we did not measure subsurface porosity at the 18 regional sites, our results suggest that subsurface weathering varies across them due to differences in bedrock composition. Mafic mineral concentrations correlate with [P] in regional granitic bedrock[35] (Fig. 4e), similar to our findings at the three main sites (Fig. 2g), implying that bedrock with higher [P] is more susceptible to weathering and produces greater porosity in soil and saprolite, all else equal. Together, our results are consistent with strong, bottom-up controls on subsurface weathering, water storage capacity, forest productivity, and dieback, due to variations in nutrient or weatherable mineral concentrations (or both) (Fig. 4f). These bottom-up bedrock controls on forests are at least as strong as top-down climatic controls and may drive a positive feedback between forest productivity and water storage capacity (Fig. 4f), if tree roots enhance

chemical[36,37] and physical weathering[30,38] that contribute to greater subsurface porosity[31]. The couplings documented here suggest that wet-year plant growth is fueled by nutrients and subsurface water and supercharged by the positive correlation between these factors in granitic bedrock of the region (Fig. 4f). This results in bedrock-driven structural overshoot and a boom-bust cycle of wet-year growth and dieback during droughts, with greater volatility in forest productivity—and greater vulnerability to drought—at sites with greater bedrock nutrient and weatherable mineral concentrations.

Acknowledgements: Funding was provided by the National Science Foundation grants EAR-1331939 (CSR) and EAR-2012357 (CSR); National Aeronautics and Space Administration grant NNX15AI08H (RPC); and Natural Sciences and Engineering Research Council of Canada grant RGPIN-2019–05501 (LSS).

Author Contributions R.P.C. and C.S.R. contributed equally to study design. R.P.C., C.S.R., and L.S.S contributed equally to manuscript preparation and revisions. R.P.C. collected the data, analyzed the data, and created the figures. K.L.F. and W.J.H. contributed to data analysis and manuscript preparation. C.S.R., L.S.S., S.P., and D.G. contributed to data analysis. N.J.T contributed to study design and field work. B.A.F. and J.L.H. contributed to field work. W.S.H. contributed to study design, field work, and manuscript preparation. All authors reviewed and commented on the manuscript.

Competing Interests: The authors declare no competing interests.

References:

1. Moore, J., Pope, J., Woods, M. & Ellis, A. 2018 Aerial Survey Results: California. (2018).
2. Stephens, S. L. *et al.* Drought, tree mortality, and wildfire in forests adapted to frequent fire. *Bioscience* **68**, 77–88 (2018).
3. Li, S. & Banerjee, T. Spatial and temporal pattern of wildfires in California from 2000 to 2019. *Sci. Rep.* **11**, 8779 (2021).
4. Wang, D. *et al.* Economic footprint of California wildfires in 2018. *Nature Sustainability* **4**, 252–260 (2020).
5. Asner, G. P. *et al.* Progressive forest canopy water loss during the 2012–2015 California drought. *Proc. Natl. Acad. Sci. U. S. A.* **113**, E249–E255 (2016).
6. Brodrick, P. G., Anderegg, L. D. L. & Asner, G. P. Forest drought resistance at large geographic scales. *Geophys. Res. Lett.* **46**, 2752–2760 (2019).
7. Jump, A. S. *et al.* Structural overshoot of tree growth with climate variability and the global spectrum of drought-induced forest dieback. *Glob. Chang. Biol.* **23**, 3742–3757 (2017).
8. Goulden, M. L. & Bales, R. C. California forest die-off linked to multi-year deep soil drying in 2012–2015 drought. *Nat. Geosci.* **12**, 632–637 (2019).
9. Paz-Kagan, T. *et al.* What mediates tree mortality during drought in the southern Sierra Nevada? *Ecol. Appl.* **27**, 2443–2457 (2017).
10. Trugman, A. T., Anderegg, L. D. L., Anderegg, W. R. L., Das, A. J. & Stephenson, N. L. Why is Tree Drought Mortality so Hard to Predict? *Trends Ecol. Evol.* (2021) doi:10.1016/j.tree.2021.02.001.
11. Goodfellow, B. W. *et al.* The chemical, mechanical, and hydrological evolution of weathering granitoid: Granite Weathering. *J. Geophys. Res. Earth Surf.* **121**, 1410–1435 (2016).
12. Shen, X., Arson, C., Ferrier, K. L., West, N. & Dai, S. Mineral weathering and bedrock weakening: Modeling microscale bedrock damage under biotite weathering. *J. Geophys. Res. Earth Surf.* **124**, 2623–2646 (2019).
13. McLaughlin, B. C. *et al.* Weather underground: Subsurface hydrologic processes mediate tree vulnerability to extreme climatic drought. *Glob. Chang. Biol.* **26**, 3091–3107 (2020).

14. Hahm, W. J. *et al.* Low subsurface water storage capacity relative to annual rainfall decouples Mediterranean plant productivity and water use from rainfall variability. *Geophys. Res. Lett.* **46**, 6544–6553 (2019).
15. Zhang, Y., Keenan, T. F. & Zhou, S. Exacerbated drought impacts on global ecosystems due to structural overshoot. *Nat Ecol Evol* **5**, 1490–1498 (2021).
16. Tague, C. & Peng, H. The sensitivity of forest water use to the timing of precipitation and snowmelt recharge in the California Sierra: Implications for a warming climate. *J. Geophys. Res. Biogeosci.* **118**, 875–887 (2013).
17. Hahm, W. J., Riebe, C. S., Lukens, C. E. & Araki, S. Bedrock composition regulates mountain ecosystems and landscape evolution. *Proc. Natl. Acad. Sci. U. S. A.* **111**, 3338–3343 (2014).
18. Uhlig, D., Schuessler, J. A., Bouchez, J., Dixon, J. L. & von Blanckenburg, F. Quantifying nutrient uptake as driver of rock weathering in forest ecosystems by magnesium stable isotopes. *Biogeosciences* **14**, 3111–3128 (2017).
19. Bateman, P. C. *Plutonism in the central part of the Sierra Nevada Batholith, California*. http://pubs.er.usgs.gov/publication/pp1483 (1992).
20. Callahan, R. P. *et al.* Arrested development: Erosional equilibrium in the southern Sierra Nevada, California, maintained by feedbacks between channel incision and hillslope sediment production. *GSA Bulletin* **131**, 1179–1202 (2019).
21. Stone, E. C. Dew as an Ecological Factor: II. The Effect of Artificial Dew on the Survival of Pinus Ponderosa and Associated Species. *Ecology* **38**, 414–422 (1957).
22. Wald, J. A., Graham, R. C. & Schoeneberger, P. J. Distribution and properties of soft weathered bedrock at ≤ 1 m depth in the contiguous United States. *Earth Surf. Processes Landforms* **38**, 614–626 (2013).
23. Klos, P. Z. *et al.* Subsurface plant-accessible water in mountain ecosystems with a Mediterranean climate. *WIREs Water* **5**, e1277 (2018).
24. Dawson, T. E., Hahm, W. J. & Crutchfield-Peters, K. Digging deeper: what the critical zone perspective adds to the study of plant ecophysiology. *New Phytol.* **226**, 666–671 (2020).
25. Rempe, D. M. & Dietrich, W. E. Direct observations of rock moisture, a hidden component of the hydrologic cycle. *Proc. Natl. Acad. Sci. U. S. A.* **115**, 2664–2669 (2018).
26. Holbrook, W. S. *et al.* Links between physical and chemical weathering inferred from a 65-m-deep borehole through Earth's critical zone. *Sci. Rep.* **9**, 4495 (2019).
27. Krone, L. V. *et al.* Deep weathering in the semi-arid Coastal Cordillera, Chile. *Sci. Rep.* **11**, 13057 (2021).
28. Callahan, R. P. *et al.* Subsurface weathering revealed in hillslope-integrated porosity distributions. *Geophys. Res. Lett.* **47**, (2020).
29. Holbrook, W. S. *et al.* Geophysical constraints on deep weathering and water storage potential in the Southern Sierra Critical Zone Observatory. *Earth Surf. Processes Landforms* **39**, 366–380 (2014).
30. Hayes, J. L., Riebe, C. S., Holbrook, W. S., Flinchum, B. A. & Hartsough, P. C. Porosity production in weathered rock: Where volumetric strain dominates over chemical mass loss. *Sci Adv* **5**, eaao0834 (2019).
31. Riebe, C. S. *et al.* Anisovolumetric weathering in granitic saprolite controlled by climate and erosion rate. *Geology* **49**, 551–555 (2021).
32. McCormick, E. L. *et al.* Widespread woody plant use of water stored in bedrock. *Nature* **597**, 225–229 (2021).
33. Vitousek, P. M., Porder, S. & Houlton, B. Z. Terrestrial phosphorus limitation: mechanisms, implications, and nitrogen–phosphorus interactions. *Ecological* **20**, 5–15 (2010).
34. Flinchum, B. A. *et al.* Estimating the water holding capacity of the critical zone using near-surface geophysics. *Hydrol. Process.* **32**, 3308–3326 (2018).
35. Bateman, P. C., Dodge, F. C. W. & Bruggman, P. E. Major oxide analyses, CPIW norms, modes, and bulk specific gravities of plutonic rocks from the Mariposa 1° x 2° sheet, central Sierra Nevada, California. *US Geological Survey Open-File Report 84--162* 49 (1984).

36. Amundson, R., Richter, D. D., Humphreys, G. S., Jobbagy, E. G. & Gaillardet, J. Coupling between Biota and earth materials in the critical zone. *Elements* **3**, 327–332 (2007).
37. Tune, A. K., Druhan, J. L., Wang, J., Bennett, P. C. & Rempe, D. M. Carbon dioxide production in bedrock beneath soils substantially contributes to forest carbon cycling. *J. Geophys. Res. Biogeosci.* **125**, (2020).
38. Gabet, E. J. & Mudd, S. M. Bedrock erosion by root fracture and tree throw: A coupled biogeomorphic model to explore the humped soil production function and the persistence of hillslope soils. *J. Geophys. Res.* **115**, (2010).

Methods:

Seismic refraction surveys

Seismic refraction surveys were conducted during the 2015 and 2016 dry seasons. We used multiple 24-channel geodes with vertical component geophones as receivers. Details about geophone deployment for each survey line are included in Supplemental Table 3. To generate seismic energy, we slammed a twelve-pound sledgehammer against a metal plate, stacking observations from multiple blows together to increase the signal-to-noise ratio. By repeating these hammer "shots" at ten-meter spacing along each survey, we generated a series of travel times for each shot-receiver combination.

To quantify vertical and lateral variations in P-wave velocity (V_P) in the subsurface, we inverted manually identified first arrival times from the geophones using a ray-tracing algorithm that minimizes the misfit between the modeled and observed travel times. The algorithm is described in detail in ref. ([39]). To estimate the robustness of the V_P inversion, we quantified the sensitivity of our results to the choice of starting model by repeating the analysis 50 times using randomly chosen starting models that range from 350 to 600 m/s in surface velocity and from 50 to 300 m/s/m in vertical velocity gradient. The average and standard deviation of V_P from the 50 models were used to estimate porosity across the survey lines.

Estimating porosity from V_P

To estimate porosity from V_P across the geophysical surveys, we used rock-physics relationships that express the subsurface as a matrix of interconnected spherical grains with interstitial pore volume less than or equal to a critical porosity that defines the threshold of suspension[40]. The rock physics model is a poro-elastic relationship based on an idealized geometric description originally developed to predict the elastic response of sedimentary reservoir rocks. Nevertheless, the model has been successfully applied to quantify subsurface porosity in weathered soil and saprolite[29,30,34,41,42]. Our model employs parameters that minimize the misfit between modeled and observed soil and saprolite porosities at a nearby calibration site[28], and was only applied to soil and saprolite, defined at our sites as material with a $V_P < 1.1$ km/s. This is the velocity at the base of saprolite at the Duff Creek site[28] and in granitic saprolite elsewhere in the western US[34].

Joint distributions of porosity and depth

To visualize subsurface weathering at each site, we condensed the collection of four saprolite porosity tomograms from each site into a single joint distribution of porosity and depth[28] (Fig. 2a-c). This approach reveals how the spread and central tendency of porosity vary with depth at each site. Site-to-site comparisons in turn show how subsurface weathering varies across the sites (c.f., Fig 2 a-c). To directly compare these joint frequency distributions, we first calculated the depth-porosity frequency distributions; then weighted them by the total depth of saprolite per meter of survey line at each site; and, finally, normalized them by the sum of the weighted distribution at Duff Creek, which had the greatest overall volume of subsurface void space. Hence, the sum of the frequency distribution at Duff Creek is one, while the sums of the distributions at Dinkey Dome and Bald Mountain each represent the amount of the subsurface weathering relative to Duff Creek. This approach accounts for variations in the volume of saprolite at each site and allows for direct comparisons of the frequency of porosity at each depth and at each site.

Unit pore volume and water storage capacity

To convert the vertical and lateral distributions of porosity from the survey lines into a metric that is relevant to vegetation, we integrated the porosity distribution vertically at each location along the surveys to obtain the total pore volume per unit area in the saprolite[29], referred to here as unit pore volume. We calculated it by integrating the rock physics-based estimates of porosity over depth from the base of saprolite (i.e., where V_P = 1.1 km s^{-1}) to the ground surface at each point along the survey lines (Extended Data Fig. 5).

Unit pore volume represents the depth of water required to fill all the void space in soil and saprolite[29]. It is the maximum amount of water that could be stored in the soil and saprolite in the absence of drainage, including water held in fine pores at pressures that prevent extraction by plants[23]. However, the site-to-site differences in unit pore volume should reliably represent site-to-site differences in water storage capacity that might buffer forests against dieback during drought given that (i) we can safely assume that the relationship between porosity and field capacity is similar across our sites due to low clay content in granitic soils at the mid elevations in the Sierra Nevada[43]; (ii) the ratio of tightly bound water to total storage capacity is low in clay-poor substrates such as those at our sites; and (iii) tree species at the sites can have roots that extend to the measured base of saprolite, as previous rooting studies have shown[44].

Geochemical and mineralogical measurements of bedrock

To quantify bedrock composition at each site, we used previously published bulk geochemical data from the Bald Mountain, Dinkey Dome, and CZO Duff (Bass Lake) (here referred to as Duff Creek) sites of ref. ([17]); bulk mineralogy from 52 additional granitic sites reported in ref. ([35]); and volumetric concentrations of quartz, potassium feldspar, plagioclase, biotite, and hornblende measured here using standard point counting techniques on thin sections created from 15 unweathered outcrop samples that we collected from Duff Creek, Dinkey Dome, and Bald Mountain (Extended Data Fig. 3). Results are reported in Supplemental Tables 1 and 2.

Quantifying evapotranspiration

We quantified evapotranspiration (*ET*) at our sites using Equation 1, a previously reported exponential relationship between Landsat-based estimates of NDVI and ground-based estimates of evapotranspiration from eddy covariance towers at sites spanning diverse ecosystems in southern California[8], including three towers within 20 km of study sites.

$$ET = 117.16e^{2.8025 \times NDVI} \quad (1)$$

Here ET is expressed in mm/yr. Since each tower's sensors were stationed above the overstory, the tower-based estimates of ET combine water vapor fluxes from the base of the canopy (i.e., the soil), the understory, and the overstory, and thus represent total forest productivity at a given point in time. Estimates of ET from Eq. 1 should likewise represent total forest productivity. The contribution of understory to leaf area index (LAI) partially explains why the relationship between ET and NDVI is exponential. As LAI increases, NDVI also increases but begins to saturate[45], because the canopy top begins to block leaf area in the understory and lower parts of the overstory. Since LAI is strongly coupled with ET through its control on water exchange with the atmosphere, we expect NDVI to also saturate with increasing ET, providing a physical basis for the exponential relationship of Eq. 1[8].

Eq. 1 allows evapotranspiration to be quantified at the 30-m resolution of Landsat pixels in areas lacking direct measurements from eddy covariance towers. It has been applied in the Sierra Nevada to quantify spatial variations in evapotranspiration[46]; temporal changes in evapotranspiration due to fire and changes in forest management[47,48]; and changes in evapotranspiration due to 2011–2017 California drought[8,49]. Here we use it to compare remotely sensed ecosystem productivity to geophysically measured subsurface weathering and geochemically inferred bedrock composition both from site to site and from location to location along individual geophysical survey lines.

To calculate yearly mean NDVI for use in calculating yearly mean ET from Equation 1, we followed methods in ref. ([8]), but averaged by calendar year, rather than by water year. All Tier 1 Landsat

5, 7, and 8 surface reflectance data for time periods between 1984 and 2018 were extracted for all center points of Landsat pixels within our study sites using Google Earth Engine. All surface reflectance data were masked for pixels with clouds, cloud shadow, and snow cover using the Landsat Quality Assurance (LQA) band in Google Earth Engine. Landsat 5 and 8 data were homogenized with Landsat 7 data using the methods of ref. ([8]) to account for slight differences in reflectance values between the different Landsat satellites[50,51]. Following homogenization, we combined time-series data for all satellites and used linear interpolation to fill data on dates masked by the LQA band. We then used the resulting yearly estimates of mean NDVI to calculate ET for each year from 1985 to 2017 using Eq. 1.

Quantifying forest dieback

We quantified dieback at each Landsat pixel as the percentage reduction in evapotranspiration from 2014 to 2016, the two years spanning the largest declines in forest health during the drought[8,52] (Extended Data Fig. 6). Dieback measured this way reflects the full spectrum of forest drought response, ranging from leaf browning to complete topkill, consistent with usage of "dieback" elsewhere in the literature[7,8]. Because dieback is calculated as the change from 2014 to 2016, positive values represent dieback and negative values represent greening due to forest growth and recovery. Because we sought to determine whether forests with greater pre-dieback evapotranspiration had disproportionately higher dieback, we quantified dieback as a percentage rather than as an absolute change in evapotranspiration.

Our analysis confirmed that forests with higher evapotranspiration had disproportionately higher dieback across our sites (Figs. 3c and 4b). To rule out the possibility that this result is an artifact of using Eq. 1 to quantify evapotranspiration from the remote sensing data, we quantified the effects of the drought using the NDVI data alone. The results confirm that our findings about bedrock controls on dieback are robust irrespective of whether dieback is measured from evapotranspiration (Figs. 3c and 4b) or NDVI (Extended Data Fig. 7).

Water and energy limitations

To quantify differences in the water and energy limitations among the sites, we calculated the aridity index, equal to the ratio of potential evapotranspiration to precipitation (PET/P), and the evaporative index, equal to the ratio of evapotranspiration to precipitation (ET/P). These indices can be used in the Budyko plotting space[53] to identify site-to-site differences in the energy and water balance (Extended Data Fig. 6). PET was estimated using the Hargreaves method[54], which requires daily estimates of mean, minimum, and maximum temperature, retrieved in this case from the PRISM Daily Spatial Climate Dataset[55]. The approach also requires daily estimates of incoming solar radiation, calculated here as a function of latitude and day of the year using the PyETo python package. Daily estimates of potential evapotranspiration were summed across all days of the year to estimate the total potential evapotranspiration for each year from 1985 to 2017. Yearly estimates of precipitation were also acquired from the PRISM Daily Spatial Climate Dataset and were corrected using a linear least-squares regression between PRISM- and gauge-based measurements of precipitation for a meteorological station close to Duff Creek[56].

Vegetation surveys

To quantify species distributions, we conducted vegetation surveys along the geophysical survey lines at each site. For each tree within five paces of a survey line, we identified the species and measured the diameter at breast height (DBH), equal to 1.37 m above the ground surface. In some cases, the species was not identifiable, because dieback during the drought led to a loss of identifying needles, cones, or both; these trees were counted and classified as "unknown." Only 6% of species were classified this way in our surveys.

Regression relationships

To quantify the relationships between evapotranspiration, dieback, and unit pore volume and evapotranspiration in Fig. 3, we used least-squares regression, with evapotranspiration and dieback

weighted by the length of geophysical survey within each Landsat pixel. This captures the degree to which average unit pore volume represents subsurface weathering across the 30-by-30-m area represented by each pixel. To account for the vertical offset between Bald Mountain and the other two sites in the log-log plotting space of Fig. 3c, we used a categorical regression with three parameters: a slope, an intercept, and an offset.

To quantify the relative importance of climate and bedrock composition in regulating evapotranspiration and dieback across the 18 sites in the regional analysis, we first used simple linear regression to gauge the individual effects of [P], MAP, and MAT, and then used multiple linear regression to gauge the combined effects of MAP and MAT and the combined effects of [P], MAP, and MAT. The results are summarized in the main text, and regression parameters, uncertainties, and p values for all regressions are reported in Extended Data Table 3.

Data Availability: Data used in this study is available via Hydroshare[57] (doi.org/10.4211/hs.edbb6ebfbc744186b5800932cd00b507) . Landsat Data can be accessed at https://www.usgs.gov/landsat-missions/landsat-data-access. PRISM climate data[55] can be accessed at https://prism.oregonstate.edu/ NAIP imagery[58] can be accessed at https://www.usgs.gov/centers/eros/science/usgs-eros-archive-aerial-photography-national-agriculture-imagery-program-naip.

Code Availability: Code used to generate figures is available on the Hydroshare repository (doi.org/10.4211/hs.edbb6ebfbc744186b5800932cd00b507). Code for geophysical and remote sensing analyses is available from the corresponding author upon request.

References (Methods only references):

39. St. Clair, J. Geophysical investigations of underplating at the Middle American Trench, weathering in the critical zone, and snow water equivalent in seasonal snow. (University of Wyoming, 2015).
40. Dvorkin, J. & Nur, A. Elasticity of high-porosity sandstones: Theory for two North Sea data sets. *Geophysics* **61**, 1363–1370 (1996).
41. Gu, X. *et al.* Seismic refraction tracks porosity generation and possible CO2 production at depth under a headwater catchment. *Proc. Natl. Acad. Sci. U. S. A.* **117**, 18991–18997 (2020).
42. Pasquet, S., Holbrook, W. S., Carr, B. J. & Sims, K. W. W. Geophysical imaging of shallow degassing in a Yellowstone hydrothermal system: Imaging Shallow Degassing in Yellowstone. *Geophys. Res. Lett.* **43**, 12,027–12,035 (2016).
43. Dahlgren, R. A., Boettinger, J. L., Huntington, G. L. & Amundson, R. G. Soil development along an elevational transect in the western Sierra Nevada, California. *Geoderma* **78**, 207–236 (1997).
44. Stone, E. L. & Kalisz, P. J. On the maximum extent of tree roots. *For. Ecol. Manage.* **46**, 59–102 (1991).
45. Carlson, T. N. & Ripley, D. A. On the relation between NDVI, fractional vegetation cover, and leaf area index. *Remote Sensing of Environment* vol. 62 241–252 (1997).
46. Goulden, M. L. *et al.* Evapotranspiration along an elevation gradient in California's Sierra Nevada: SIERRA NEVADA EVAPOTRANSPIRATION. *J. Geophys. Res.* **117**, (2012).
47. Ma, Q. *et al.* Wildfire controls on evapotranspiration in California's Sierra Nevada. *J. Hydrol.* **590**, 125364 (2020).
48. Roche, J. W., Goulden, M. L. & Bales, R. C. Estimating evapotranspiration change due to forest treatment and fire at the basin scale in the Sierra Nevada, California: Forest Disturbance and Evapotranspiration Change. *Ecohydrol.* e1978 (2018) doi:10.1002/eco.1978.
49. Bales, R. C. *et al.* Mechanisms controlling the impact of multi-year drought on mountain hydrology. *Sci. Rep.* **8**, 690 (2018).
50. Roy, D. P. *et al.* Characterization of Landsat-7 to Landsat-8 reflective wavelength and normalized difference vegetation index continuity. *Remote Sens. Environ.* **185**, 57–70 (2016).
51. Su, Y. *et al.* Emerging stress and relative resiliency of giant sequoia groves experiencing multiyear

dry periods in a warming climate: Emerging stress of giant sequoia groves. *J. Geophys. Res. Biogeosci.* **122**, 3063–3075 (2017).
52. Moore, J., McAfee, L. & Iaccarino, J. 2016 Aerial Survey Results: California. (2017).
53. Budyko, M. I., Miller, D. H. & Miller, D. H. *Climate and life*. vol. 508 (Academic press New York, 1974).
54. Hargreaves, G. H. & Samani, Z. A. Reference crop evapotranspiration from temperature. *Appl. Eng. Agric.* **1**, 96–99 (1985).
55. PRISM Climate Group. PRISM Climate Data. *Oregon State University* (2019).
56. Bales, R. *et al.* Spatially distributed water-balance and meteorological data from the rain–snow transition, southern Sierra Nevada, California. *Earth Syst. Sci. Data* **10**, 1795–1805 (2018).
57. Callahan, R. P. Supplement for 'Forest vulnerability to drought controlled by bedrock composition'. *Hydroshare* (2022).
58. Earth Resources Observation and Science (EROS) Center. National Agriculture Imagery Program (NAIP). (2017) doi:10.5066/F7QN651G.

Extended Data Figures and Tables:

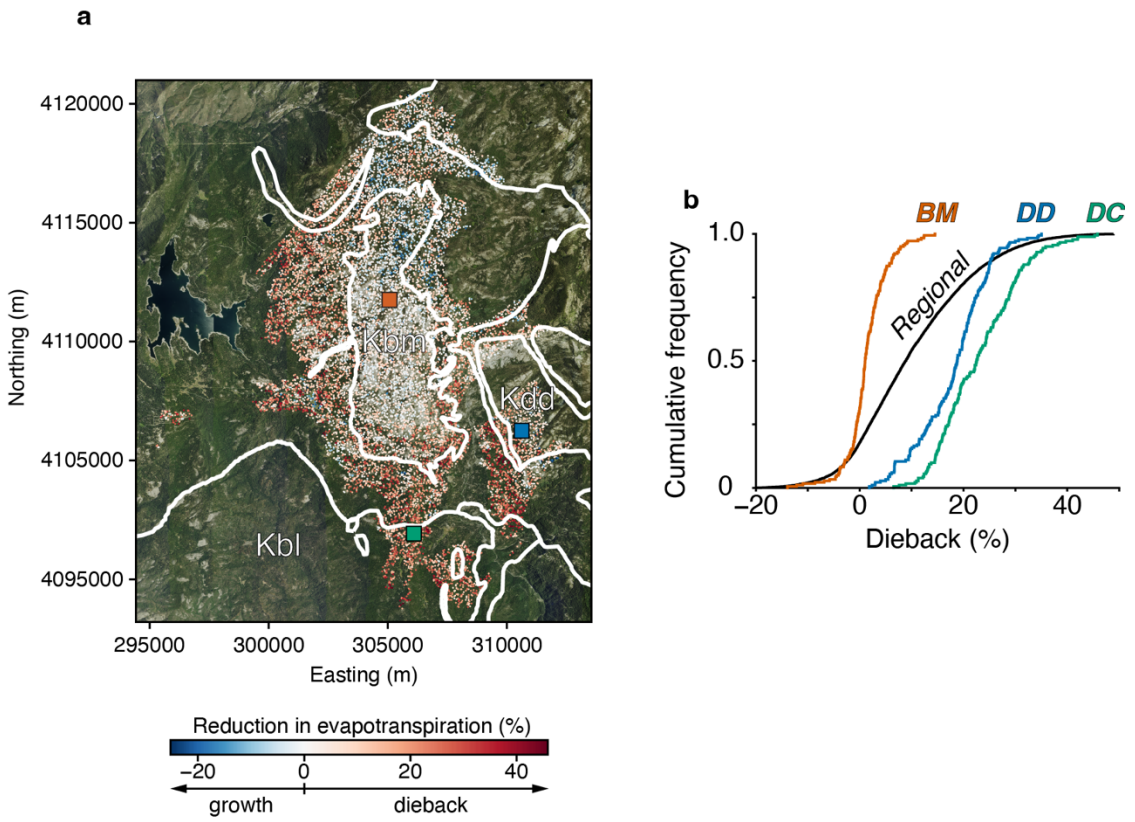

Extended Data Fig. 1 | Forest dieback in the region around the study sites. a, Percentage reduction in evapotranspiration from 2014 to 2016 (colorbar) across a 14,876-pixel subset of nearby Landsat pixels (colored squares) with elevations between 1800 and 2400 m but still outside the extent of Pleistocene glaciation. NAIP imagery from 2014 (background) shows differences in vegetation density and white lines represent boundaries between bedrock types (Kbm is Bald Mountain Granite; Kdd is Dinkey Dome Granite; Kbl is Bass Lake Tonalite). **b,** The distribution of dieback differs markedly between the sites ($p < 0.0001$ for all three comparisons in a two-sample K-S test after adjusting for multiple comparisons) and collectively spans 94% of the range in dieback spanned by the surrounding region (black).

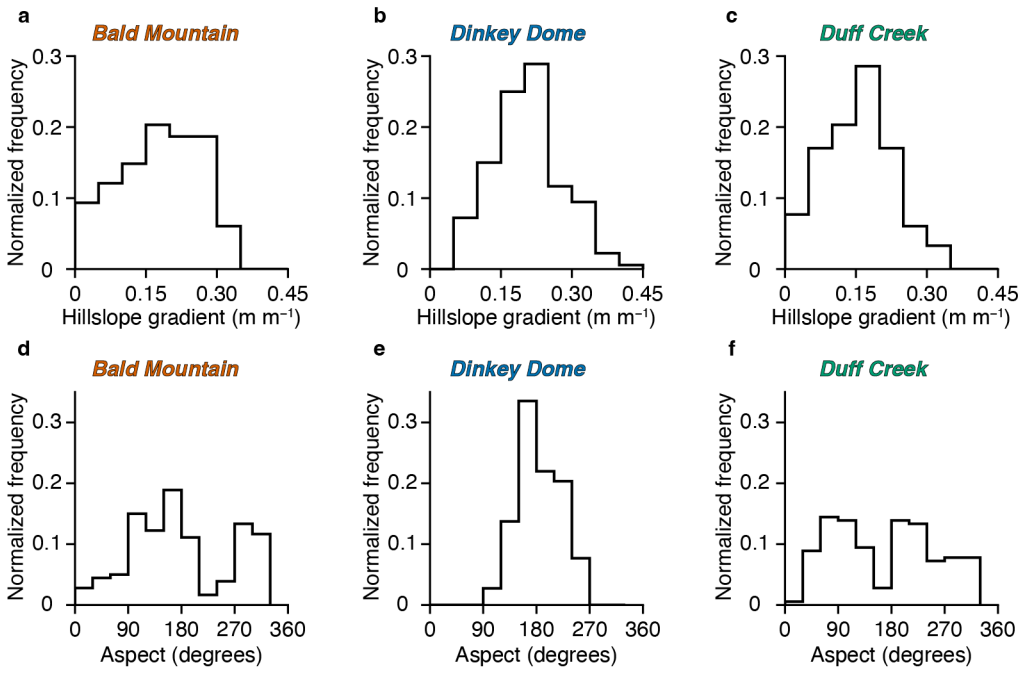

Extended Data Fig. 2 | Topography at study sites. Study sites are located on ridgetops and therefore have gentle hillslope gradients (with most <30%) (**a-c**) and have surfaces pointing in multiple directions, leading to wide distributions in slope aspect (**d-f**).

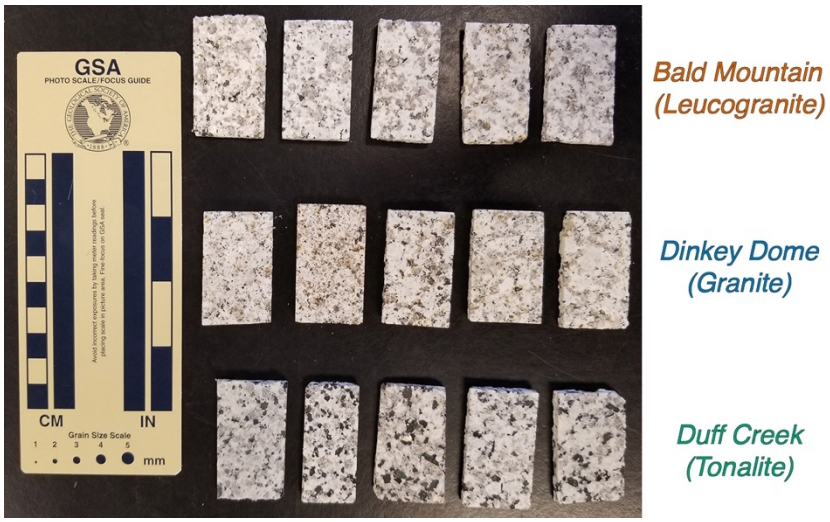

Extended Data Fig. 3 | Variations in bedrock composition. Thin sections cut from bedrock sampled at each of the study sites in Fig. 1. We quantified bulk mineralogy from these thin sections using standard point-counting techniques (see Methods; Fig. 1b; Supplemental Tables 1 and 2).

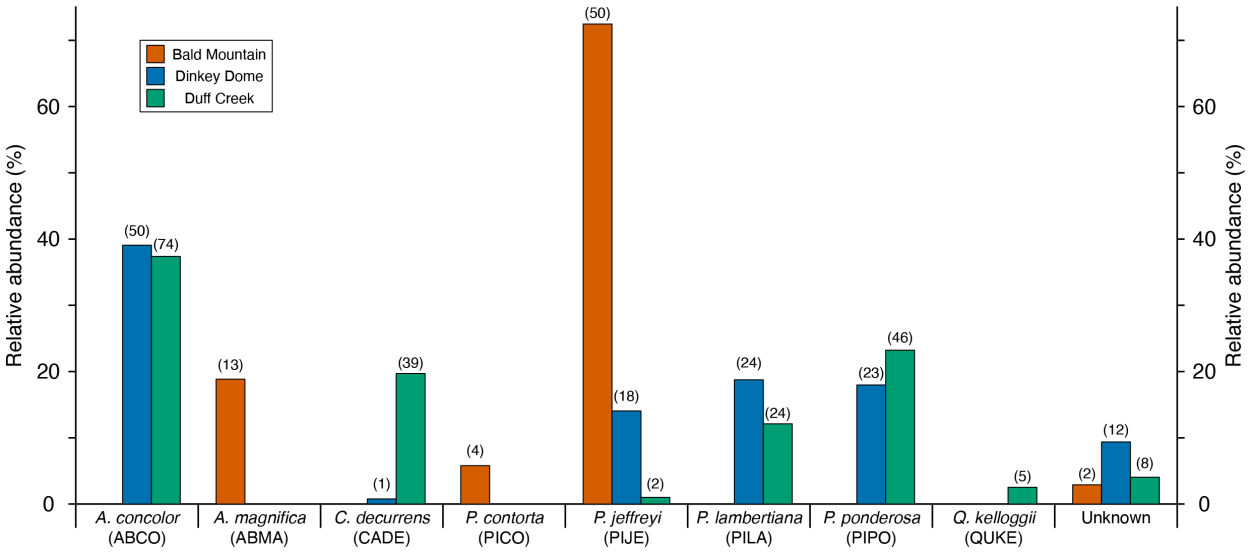

Extended Data Fig. 4 | Vegetation surveys. Relative abundance of the eight species identified in surveys at the three study sites in Fig 1 (see Methods). Numbers in parentheses are the number of individuals found at each site. Some trees were not identifiable due to a dieback-related lack of needles or pine cones, so numbers do not sum to 100% at any site.

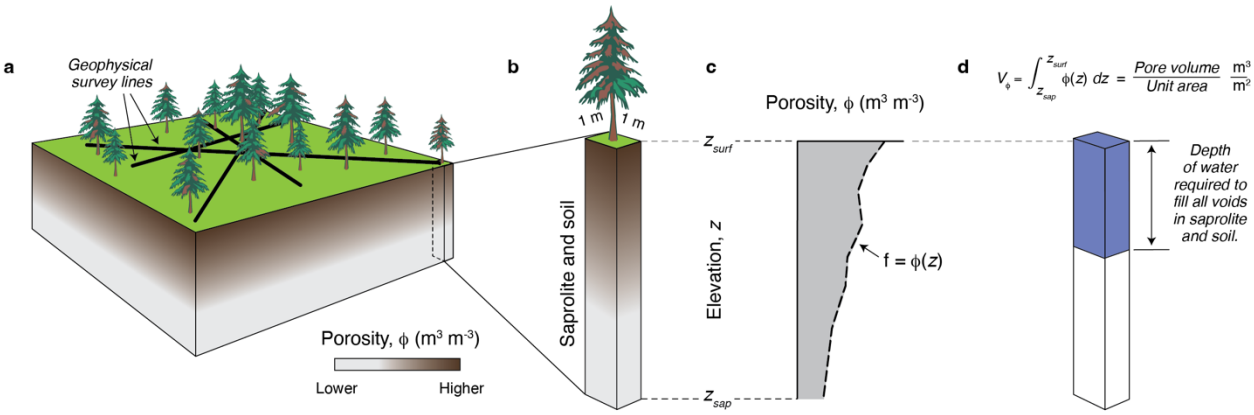

Extended Data Fig. 5 | Calculating unit pore volume. a, Idealized landscape with geophysical transects (black lines) at surface above weathered soil and saprolite with a vertical gradient in porosity. **b,** 1×1 m plot and underlying column of soil and saprolite spanned by the survey. **c,** Unit pore volume (φ_v) is calculated by integrating geophysics-based porosity ($\varphi(z)$, gray shaded area) over depth (z) between the base of saprolite (z_{sap}) and the surface (z_{surf}), where z_{sap} is defined by a threshold V_P = 1.1 km/s (see Methods). **d,** We define unit pore volume as the total pore volume per unit area at the surface. It therefore represents the depth of water required to fill all the void space in the column of soil and saprolite in panel b.

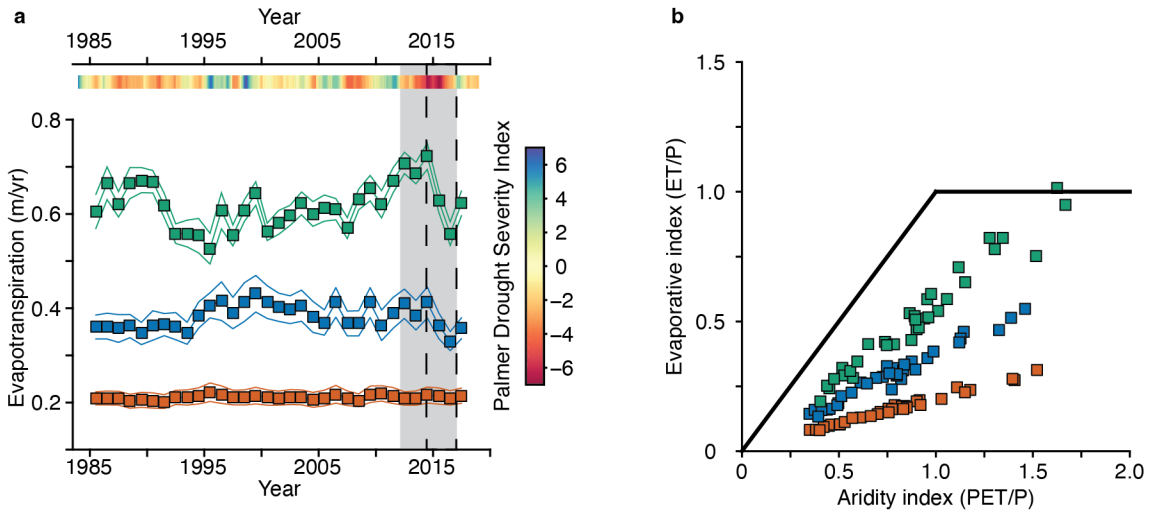

Extended Data Fig. 6 | Drought effects on water and energy balances. a, Variations in evapotranspiration through time at three main study sites with Palmer Drought Severity Index[57] (top) and gray band highlighting 2011-2017 California drought. Dashed lines span the 2014 and 2016 interval in which forests experienced the greatest declines in evapotranspiration. Although the drought began in late 2011, forests at our sites did not experience a marked decline in evapotranspiration until 2015. **b,** Site-to-site differences in evapotranspiration and similarities in climate drive differences in evaporative index (evapotranspiration divided by precipitation) for a given aridity index (potential evapotranspiration divided by precipitation). Points are water-year averages. Bold lines mark Budyko's energy and water limitations on evapotranspiration when runoff is negligible[53]. Points above and just beneath the water limit indicate plants used water stored during prior wet years.

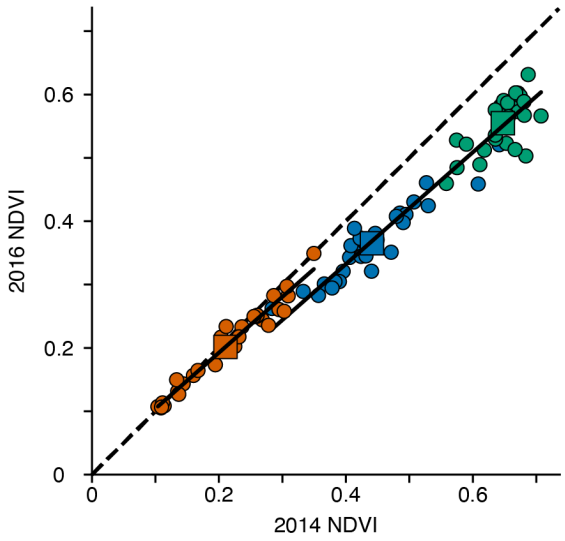

Extended Data Fig. 7 | Drought-related dieback from NDVI. NDVI data from 2014 to 2016 generally plot below 1:1 line, indicative of drought-related declines at all 3 sites. Like the ET-ET plot in the main text (Fig. 3c), the data are consistent with a three parameter regression, with a slope, an intercept, and an offset between Bald Mountain and the other two sites (see Extended Data Table 3 for regression parameters, uncertainties, and p values). The statistically significant offset is consistent with a species-related control on forest dieback, as discussed in the main text. In addition, the slope of the relationship is not ≥1 ($p<0.0001$), so we can reject the null hypothesis that greater water storage capacity at sites with

higher pre-dieback forest productivity compensates for the higher water demand. Hence, dieback from NDVI increases disproportionately with increasing pre-dieback NDVI. Moreover, our results are consistent with bedrock control of dieback, irrespective of whether dieback is quantified using NDVI or ET derived from NDVI.